



## Foreland uplift during flat subduction: Insights from the Peruvian Andes and Fitzcarrald Arch

Brandon T. Bishop<sup>a,\*</sup>, Susan L. Beck<sup>a</sup>, George Zandt<sup>a</sup>, Lara S. Wagner<sup>b</sup>, Maureen D. Long<sup>c</sup>, Hernando Tavera<sup>d</sup>

<sup>a</sup> Department of Geosciences, University of Arizona, 1040 East 4th Street, Tucson, AZ 85721, USA

<sup>b</sup> Department of Terrestrial Magnetism, Carnegie Institution for Science, 5241 Broad Branch Road NW, Washington, DC 20015, USA

<sup>c</sup> Department of Geology and Geophysics, Yale University, 210 Whitney Avenue, New Haven, CT 06511, USA

<sup>d</sup> Instituto Geofísico del Perú, Calle Badajoz 169, Lima 15012, Peru

### ARTICLE INFO

#### Keywords:

Basal shear  
Flat slab  
Andes  
Crustal thickening  
Lithosphere  
Fitzcarrald Arch

### ABSTRACT

Foreland deformation has long been associated with flat-slab subduction, but the precise mechanism linking these two processes remains unclear. One example of foreland deformation corresponding in space and time to flat subduction is the Fitzcarrald Arch, a broad NE-SW trending topographically high feature covering an area of  $> 4 \times 10^5 \text{ km}^2$  in the Peruvian Andean foreland. Recent imaging of the southern segment of Peruvian flat slab shows that the shallowest part of the slab, which corresponds to the subducted Nazca Ridge northeast of the present intersection of the ridge and the Peruvian trench, extends up to and partly under the southwestern edge of the arch. Here, we evaluate models for the formation of this foreland arch and find that a basal-shear model is most consistent with observations. We calculate that  $\sim 5 \text{ km}$  of lower crustal thickening would be sufficient to generate the arch's uplift since the late Miocene. This magnitude is consistent with prior observations of unusually thickened crust in the Andes immediately south of the subducted ridge that may also have been induced by flat subduction. This suggests that the Fitzcarrald Arch's formation by the Nazca Ridge may be one of the clearest examples of upper plate deformation induced through basal shear observed in a flat-slab subduction setting. We then explore the more general implications of our results for understanding deformation above flat slabs in the geologic past.

### 1. Introduction

The link between flat-slab subduction and the associated overriding plate's response has been the focus of many studies of both modern and ancient flat slabs (e.g. Ramos and Folguera, 2009; Sébrier et al., 1988; Yonkee and Weil, 2015). Many models of flat-slab subduction (e.g. Dickinson and Snyder, 1978; Humphreys et al., 2015; Noury et al., 2017) have assumed that, inboard of the forearc, the top of sub-horizontal slabs remained at a depth of  $\sim 100 \text{ km}$  to  $200 \text{ km}$  along the base of the overriding plate's lithosphere before re-steepening to descend into the deeper mantle. While this configuration could transmit compressive stress to the overriding plate and cause faulting in the crust of the backarc or foreland (e.g. Dickinson and Snyder, 1978; Sébrier et al., 1988; Yonkee and Weil, 2015; though see Margirier et al., 2017 for a complicating view), these models did not call for the slab to directly modify the mid-to-lower continental crust inboard of the forearc. In the context of modern flat-slab occurrences, these models are consistent with observations of the slab's spatial relationship to the broken

foreland (i.e. basement cored uplifts) associated with the Chilean-Argentine Sierras Pampeanas flat slab (e.g. Jordan and Allmendinger, 1986; Ammirati et al., 2015). However, observations of the Peruvian flat slab (e.g. Bishop et al., 2017) and Argentina Precordillera (the western portion of the Pampean flat-slab region, Allmendinger and Judge, 2014), suggest that these models do not provide an adequate explanation for all examples of upper plate deformation associated with flat-slab subduction.

The southern segment of the Peruvian flat slab extends horizontally for  $\sim 500 \text{ km}$  northeast and inboard from the trench (Antonijevic et al., 2015; Barazangi and Isacks, 1976; Gutscher et al., 1999; Gutscher et al., 2000; Scire et al., 2016), with the shallowest portion directly in line with the projected location of the  $200 \text{ km}$  wide subducted Nazca Ridge. The oceanic Moho of the subducted slab, as determined by receiver functions, lies at  $< 80 \text{ km}$  depth. The overriding continental Moho lies at  $\sim 50\text{--}55 \text{ km}$  depth (Bishop et al., 2017). Given that the oceanic crust of the Nazca Ridge offshore is  $\sim 18 \text{ km}$  thick (Hampel et al., 2004; Woods and Okal, 1994), this suggests that the continental mantle

\* Corresponding author.

E-mail address: [brandontbishop@email.arizona.edu](mailto:brandontbishop@email.arizona.edu) (B.T. Bishop).

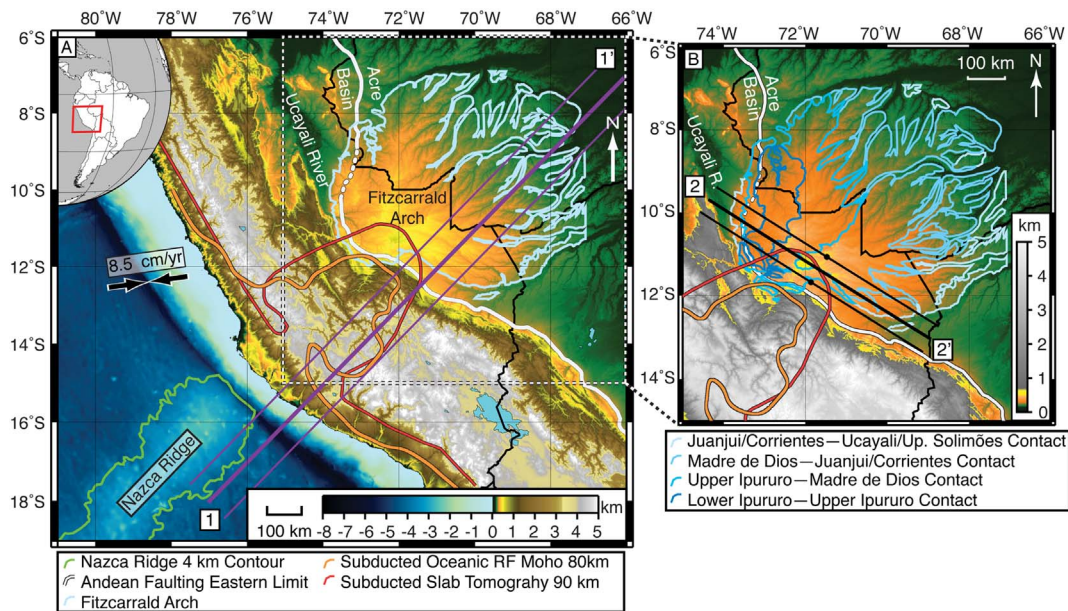


**Fig. 1.** A: Tectonic setting of the Fitzcarrald Arch. Globe hemisphere inset marks study area. Blue line is boundary of uplifted Miocene to Pleistocene units associated with the arch (from Espurt et al., 2010). White line is inboard boundary of Andean faulting (modified from Hermoza et al., 2006; Gautheron et al., 2013; McQuarrie et al., 2008). Orange line is 80 km depth contour of subducted Nazca oceanic crustal Moho (from Bishop et al., 2017). Red line is 90 km depth contour for subducted Nazca plate based on surface-wave tomographic anomaly (Antonijevic et al., 2015). Green line is the outline of the unsubducted segment of the Nazca Ridge (from Hampel, 2002). Purple line 1–1' marks location of geophysical cross-section in Fig. 2 and was selected because it is coincident with the densest line of seismic stations. The 5 to 0 Ma average convergence of 8.5 cm/yr between South American and Nazca Plates (black arrows) is from Somoza and Ghidella (2012). Topography from Global Multi-Resolution Topography (GMRT) v.3.2 (Ryan et al., 2009). B: Topographic and geologic expression of Fitzcarrald Arch. Light blue to dark blue lines are uplifted and exposed Pliocene (light blue) to mid-Miocene (dark blue) sedimentary units (from Espurt et al., 2010). Line 2–2' show location of topographic profile in Figs. 3 and 4, lines with black dots parallel to 2–2' mark swath used to obtain averaged topography in Figs. 3 and 4. (For interpretation of the references to color in this figure legend, the reader is referred to the web version of this article.)

lithosphere, and possibly portions of the lower continental crust, have been removed or displaced by this segment of the Peruvian flat slab (Bishop et al., 2017). The ongoing deformation of the overriding plate associated with the southern portion of the Peruvian flat slab near the subducted Nazca Ridge represents an analogue for similar flat slab processes whose records of deformation have been preserved in the geologic record. One example of this comes from the recent discovery of forearc-derived schists originally emplaced at mid-to-lower crustal depths during the North American Cretaceous–Paleogene Laramide flat slab in western Arizona (Haxel et al., 2015). These schists have been interpreted as the top of the Laramide subduction interface (Haxel et al., 2015). This requires the complete removal of the lower continental crust several hundred kilometers inboard of the Cretaceous–Paleogene trench. In both locations, this lower crustal deformation requires significant lateral displacement of lithospheric mantle and mid-to-lower crust.

In this study, we investigate the Peruvian foreland where a broad uplift, the Fitzcarrald Arch, is present (Fig. 1). The Fitzcarrald Arch is a broad, dome-like uplift ENE of the Andean deformation front within the Amazonia foreland that lies above and inboard of the flat slab, in line with the projection of the subducted Nazca Ridge (Espurt et al., 2007a). The uplift of the Fitzcarrald Arch has been ongoing over the last ~4 Myrs, contemporaneous with subduction of the Nazca Ridge and formation of the flat slab in this part of Peru (Espurt et al., 2007a). We evaluate existing explanations for the formation of the Fitzcarrald Arch (i.e. Espurt et al., 2007a; Regard et al., 2009; Dávila and Lithgow-Bertelloni, 2015) that principally focus on dynamic and isostatic effects associated with a buoyant subducted Nazca Ridge. Based on new seismic constraints on the geometry of the flat slab, we also consider two additional possible mechanisms for the arch's formation: 1) uplift due to serpentinization and 2) uplift caused by basal shear and crustal thickening. We calculate the extent of rock uplift (including eroded material) represented by the arch and use this to constrain the most likely mechanism for the formation of the Fitzcarrald Arch.

### 1.1. Geologic background

The Fitzcarrald Arch has a maximum elevation ~500 m above the surrounding basins and covers an area of  $\sim 4 \times 10^5$  km<sup>2</sup>. The initiation of the Fitzcarrald Arch's uplift is consistent with onset of flat-slab subduction in the region (Espurt et al., 2010; Hampel, 2002). The Amazonia foreland inboard of the Peruvian flat slab may be divided into two segments based on deformation style (Fig. 1A). North of ~11.5°S, the eastern extent of Andean thrusting shifts eastward from the thin-skinned Subandes (Gautheron et al., 2013) to incorporate reactivated Paleozoic faults as far east as the Acre Basin (e.g. Hermoza et al., 2006). The Fitzcarrald Arch lies east of these faults and is characterized by little to no Cenozoic surface faulting (Espurt et al., 2007a; Gautheron et al., 2013) despite the uplift and erosion of Miocene tidal deltaic and estuarine deposits (Espurt et al., 2010; see Fig. 1B for locations of sedimentary units).

Early interpretations of the arch as the product of propagation of Subandean folding and faulting (Dumont et al., 1991) or reactivation of Paleozoic or earlier structures (Jacques, 2003) are inconsistent with the truncation of basement faults by a Cretaceous erosional unconformity and the lack of significant faulting in Cenozoic strata as interpreted from seismic reflection and well data (Espurt et al., 2007a, 2010). The interpretation of the arch as an alluvial megafan (Picard et al., 2008) is inconsistent with the observed pattern of drainage networks on the arch, the uplifted Mesozoic strata approximately paralleling the arch's topography, and the arch's comparatively high characteristic slope (Regard et al., 2009). These observations are, however, consistent with the interpretation of the arch as a Pliocene to present crustal upward resulting from the subduction of the Nazca Ridge (Espurt et al., 2007a, 2010). The aseismic Nazca Ridge comprises ~18 km thick oceanic crust that has been subducting along the Peruvian Trench for at least ~11 Myrs (Hampel, 2002; Hampel et al., 2004) and possibly for ~15 Myrs (Rosenbaum et al., 2005). The subduction of the Nazca Ridge is a contributing factor to flat subduction, which has resulted in the

termination of the overlying volcanic arc since ~3–4 Ma (Rosenbaum et al., 2005). According to Espurt et al. (2010), the arch developed after a switch in the foreland basin from Miocene (~9 Ma) tidally influenced to Pliocene (~3 Ma) fluvial conditions. The resulting uplift led to ~700 m of Miocene deposits being removed from the eastern side of the arch (Espurt et al., 2010) and 400 m to 500 m of surface uplift relative to the surrounding foreland basin (Espurt et al., 2007a). The timing and southeastward propagation of the arch's growth is consistent with the predicted arrival of the subducted Nazca Ridge and onset of the associated flat slab subduction in the region (Antonijevic et al., 2015; Espurt et al., 2010; Hampel, 2002).

While studies using global teleseismic earthquake locations have previously identified the rough geometry of the Peruvian flat slab (e.g. Barazangi and Isacks, 1976; Gutscher et al., 1999; Gutscher et al., 2000) the recent temporary deployment of seismic arrays containing > 140 broadband seismic stations in southern Peru have provided the opportunity to develop a much more detailed understanding of the slab's geometry between ~10.5°S and ~17°S, directly over and adjacent to the location of the subducting Nazca Ridge. Receiver function and tomographic studies (Antonijevic et al., 2015; Bishop et al., 2017; Scire et al., 2016) utilizing these deployments have shown that the subducting Nazca oceanic plate remains nearly flat at a depth of < 80 km along the inboard projection of the Nazca Ridge before plunging at a high angle (~70°) into the mantle. While there is still some uncertainty on the exact location where the slab starts to re-subduct, these new results suggest that the northeastern most extent of the flat slab associated with the subducted ridge may extend partly under the southwestern edge of the Fitzcarrald Arch (Fig. 1A, B).

## 2. Proposed mechanisms for the formation of the Fitzcarrald Arch

The spatial correspondence between the unsubducted Nazca Ridge, the shallow portion of the flat slab, and the Fitzcarrald Arch is readily evident (see Fig. 1A). However the mechanisms responsible for the arch's uplift are still debated. Limited Cenozoic faulting on the arch, its large spatial half-wavelength (> 500 km), and its low amplitude indicate involvement of the entire crust or lithosphere (Espurt et al., 2007a, 2007b). Three mechanisms for arch uplift have been proposed: (1) dynamic subsidence of the surrounding basins (Espurt et al., 2007a); (2) dynamically and isostatically induced uplift due to the buoyant oceanic crust of the subducted Nazca Ridge (Dávila and Lithgow-Bertelloni, 2015); and (3) a combination of subducted ridge buoyancy and plate coupling (Regard et al., 2009). We consider each of these models in light of new seismic constraints on the geometry of the flat slab, and then discuss additional possible mechanisms for the arch's formation.

The first model links the deep geometry of the subducted slab to the deformation observed at the surface through dynamic topography. Espurt et al. (2007a) propose that the uplift of the Fitzcarrald Arch is due in part to the dynamic subsidence of its surrounding basins. This mechanism follows the numerical model of Pysklywec and Mitrova (2000) that found that stagnation of a subducting slab at the base of the mantle transition zone at 660 km depth could produce areas of isolated dynamic uplift within a larger region of dynamic subsidence. However, recent teleseismic tomography (Scire et al., 2017; see Fig. 2) finds that the subducting plate beneath the Central Andes penetrates through the mantle transition zone to at least 900 km depth, indicating this model is not applicable to the Fitzcarrald Arch.

The second model (e.g. Espurt et al., 2007a; Dávila and Lithgow-Bertelloni, 2015) suggests that the Fitzcarrald Arch may have developed due to neutral or positive buoyancy of the flat slab associated with the subducted Nazca Ridge even though much of the arch lies northeast of the flat slab and the slab descends steeply into the mantle towards the arch's southwestern edge (Fig. 2A). Dávila and Lithgow-Bertelloni (2015) propose a dynamic topography model for the entire South American margin that also incorporates the potential isostatic effects of

lithospheric density variations in the slab and overriding plate. In their model the crust of the subducted Nazca Ridge remains un-eclogitized, and thus positively buoyant, despite being subjected to eclogite-facies pressure and temperature conditions (metastable). The additional buoyancy from the thick un-eclogitized crust of the Nazca Ridge produces localized uplift that they suggest can explain the uplift of the Fitzcarrald Arch.

The existence of metastable subducted oceanic crust has been proposed as an important contributing (if not sufficient) factor in the formation of flat subduction (e.g. Arrial and Billen, 2013; Van Hunen et al., 2002). Other numerical models (e.g. Currie and Beaumont, 2011; Manea et al., 2012) indicate that factors including overthrusting of the upper plate and mantle wedge suction forces are capable of inducing flat subduction even in eclogitized slabs, suggesting that un-eclogitized crust is not a necessary component of flat slab subduction. Receiver function analysis indicates that the subducted Nazca Ridge crust becomes significantly eclogitized < 400 km from the Peruvian Trench (Bishop et al., 2017; see Fig. 2), ~300 km west of the arch. This suggests that alternative sources of buoyancy may support the eastern extent of the flat slab. A low velocity body beneath the subducted Nazca Ridge imaged in teleseismic (Scire et al., 2016) and surface-wave (Antonijevic et al., 2015; Antonijevic et al., 2016) tomography has been suggested to provide additional support for the flat slab (Antonijevic et al., 2016). The ability of this low velocity body to support the inboard extent of the flat slab, much less the uplift of the overriding portions of the Fitzcarrald Arch or the arch's northeast extension, is poorly constrained without more detailed geodynamic modeling of the newly determined slab geometry. However, given that most models of flat slab subduction suggest subsidence is more likely than uplift (e.g. Eakin et al., 2014a), we currently consider this model less likely than those discussed below to be responsible for the arch's uplift.

The third model relates the uplift of the arch to purely isostatic forces. These isostatic mechanisms of arch uplift invoke a decrease in the average density of the overriding lithosphere (e.g. due to the partial serpentinization of the overriding lithospheric mantle or due to the thickening of the middle to lower continental crust resulting from basal shear). Similar mechanisms have been suggested to explain deformation associated with Laramide flat-slab subduction and the deformation associated with Pampean flat-slab subduction.

Density decrease and volume increase due to hydration-induced serpentinization of lithospheric mantle during flat subduction has been invoked as a mechanism for weakening the lithosphere of western North America and uplifting the Colorado Plateau during Laramide flat subduction (e.g. Schulze et al., 2015). Similarly, for the Pampean flat slab, a low shear-wave velocity region in the mantle above the Sierras Pampeanas flat slab may indicate a similar hydration event, although no surface uplift has been linked to this process (Porter et al., 2012). The role of such serpentinization on the uplift of the Fitzcarrald Arch has not previously been investigated in the literature in detail. We investigate these effects (Section 4.1) and discuss the applicability of this mechanism to this particular tectonic setting.

The creation of topography through localized basement cored thrusting of the overriding plate's crust due to increased plate coupling above a flat slab has been proposed as a mechanism to explain foreland deformation in the Sierras Pampeanas above the present Chile-Argentinian flat slab (e.g. Jordan and Allmendinger, 1986) and in Laramide structures above the proposed Cretaceous to mid-Cenozoic Farallon flat slab beneath parts of western North America (e.g. Dickinson and Snyder, 1978). In both locations, interplate coupling has been used to explain the formation of basement cored uplifts—structures which are characterized by faults that place basement rock on younger sedimentary units with spatial wavelengths of 100 s of meters to 10s of kilometers (e.g. compilation in Bump, 2003).

Recent seismic observations of the southern margin of the Peruvian flat slab associated with the subducting Nazca Ridge indicate that the overriding and subducting plates are coupled in this location to a

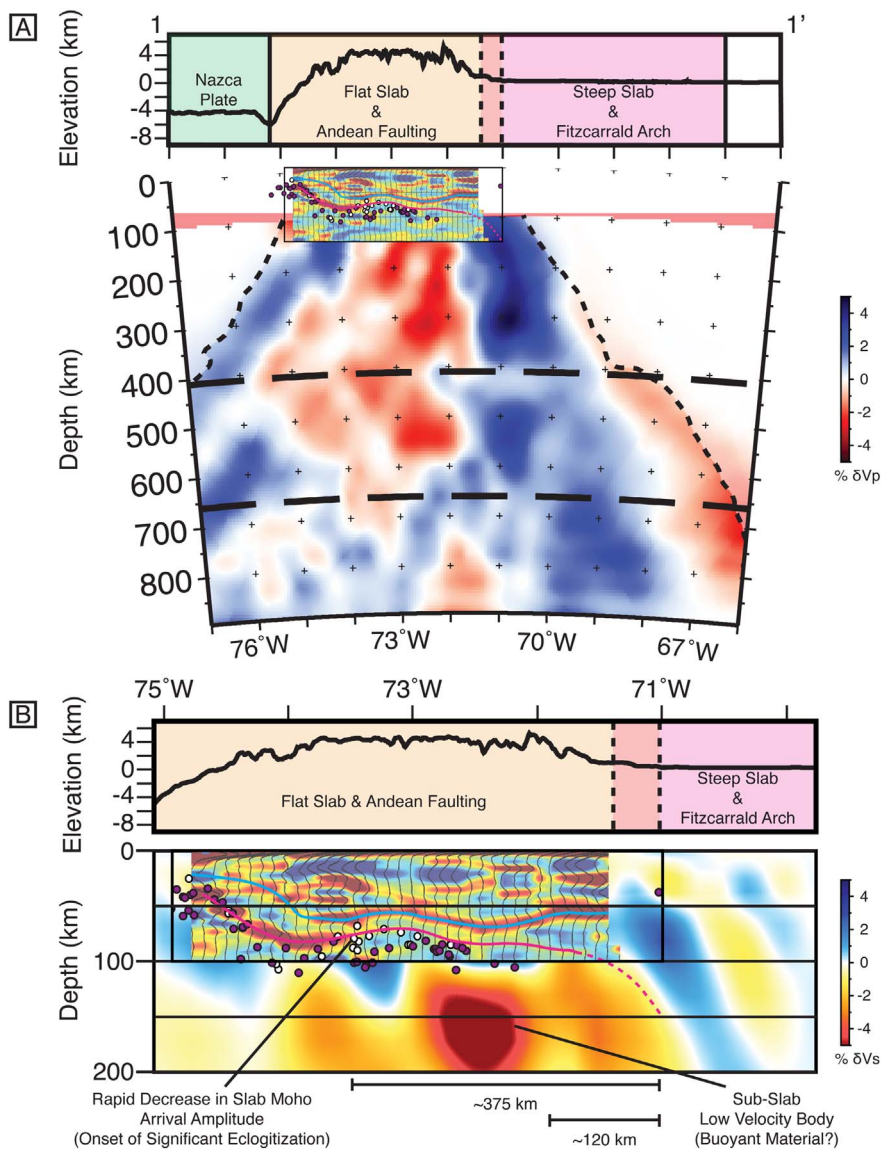


**Fig. 2.** Geophysical cross-section through segment of flat slab along profile 1–1' in Fig. 1A combining P-wave teleseismic tomographic results (modified from Scire et al., 2017), surface (shear) wave tomography results (replotted from Antonijevic et al., 2015), and P-wave receiver function results (modified from Bishop et al., 2017). Color of tomography results represents percent differences from starting model. A: Receiver function results scaled to teleseismic tomography results. Filled circles mark location of slab seismicity as shown in Scire et al. (2017) and Bishop et al. (2017) (purple and white fill respectively). Blue line in receiver function results marks the Bishop et al.'s (2017) continental Moho while the magenta line marks the subducted slab oceanic Moho (dashed where inferred). The near vertical high-velocity feature near 70°W marks the steeply dipping slab immediately inboard of the area of flat subduction (Scire et al., 2017). This high velocity feature penetrates into the lower mantle (> 660 km depth) without flattening at the base of the mantle transition zone. The slab hinge marking the transition from flat to steep subduction occurs near the present eastern edge of Andean faulting, indicating the slab cannot provide direct support to the entire Fitzcarrald Arch. B: Receiver function results scaled to surface wave tomography results. Rapid decrease in slab Moho amplitude indicates a decrease in the velocity contrast between the subducted slab crust and underlying slab mantle, consistent with the onset of significant eclogitization > 300 km from the Fitzcarrald Arch (Bishop et al., 2017). A weak slab Moho arrival continues to the location of the slab hinge as inferred from the tomography results before becoming indistinguishable from other arrivals. The similar geometries of the continental and slab Mohos and < 20 km separation between the features throughout the flat slab region indicates strong coupling between the two plates. Surface wave results indicate that the slab begins to re-steepen in the transitional area between the Subandes and the Fitzcarrald Arch, > 100 km east of a sub-slab slow velocity, potentially buoyant, mantle anomaly. (For interpretation of the references to color in this figure legend, the reader is referred to the web version of this article.)

degree that appears to exceed the hypothesized general increase in plate coupling associated with the whole of the Peruvian flat slab (e.g. Gutscher et al., 2000; Martinod et al., 2010). The localization of coupling above the subducted Nazca Ridge is also consistent with models that call for changes in the location and degree of coupling above the Peruvian flat slab through time (e.g. Margirier et al., 2017). Around the subducted ridge, the slab's oceanic Moho and the overriding continental Moho in the region within the Andes west of the arch appear to parallel each other with a separation of < 20 km (Bishop et al., 2017; Ma and Clayton, 2015), implying strong mechanical coupling. This observation is consistent with Regard et al. (2009) who suggest that increased plate coupling above the subducted Nazca Ridge may have helped to form the Fitzcarrald Arch. However, we note that crustal thickening related to the arch must occur on a spatial scale more than an order of magnitude broader than the thickening documented in the basement cored uplifts of other settings and without any associated faulting of the upper crust. This suggests that the surface and upper crustal expression of crustal thickening may be significantly influenced by characteristics of the overriding plate (e.g. alignment of pre-existing faults (Gautheron et al., 2013; Eude et al., 2015)). Given the difference between the observed uplift above the southern part of the Peruvian flat slab and those seen above other flat slabs, we investigate the possible effects of basal-shear-induced crustal thickening on the uplift of the Fitzcarrald Arch

(Section 4.2) in order to better understand the relationship between this surface uplift and the recently improved constraints on the underlying flat slab's geometry.

### 3. Methods for quantifying arch uplift

Before we can investigate new models for the formation of the Fitzcarrald Arch, we must first quantify the amount and location of rock uplift experienced by the arch. The present topography of the Fitzcarrald Arch does not represent the full uplift of the arch; a significant amount (~1 km) of sedimentary rock has been eroded from the northwest portion of the arch (Espurt et al., 2007a; see Fig. 1). This material must be accounted for when calculating rock uplift. In establishing the timing of the uplift of the Fitzcarrald Arch, Espurt et al. (2007a, 2010) identified a set of unit contacts that may be used as an initial set of benchmarks to constrain the magnitude of the arch's uplift. We build on these benchmarks to calculate the geometry of the arch's rock uplift relative to the surrounding basins (Section 3.1).

In conjunction with existing lithospheric plate parameters calculated for the region, the geometry of rock uplift allows us to evaluate the mechanism for arch formation. We describe how we quantify the amount of uplift that might be expected from mantle serpentinization (Section 3.2.1) or crustal thickening due to basal shear (Section 3.2.2).

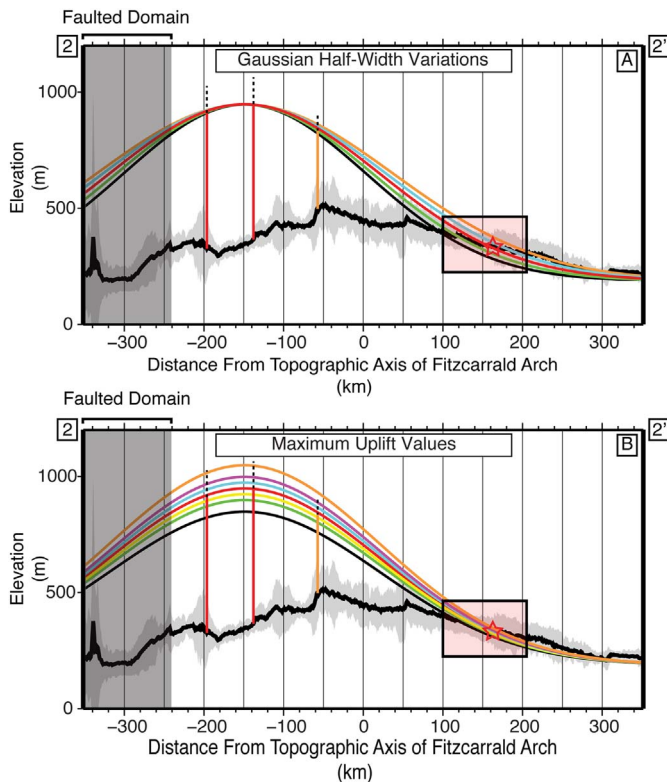


**Fig. 3.** Comparison of alternate Gaussian models used to approximate the uplifted Miocene surface associated with the development of the Fitzcarrald Arch. Vertical lines mark calculated elevation of contact uncorrected for isostatic unloading (dashed black lines) and corrected for isostatic unloading (solid red and orange lines). This correction accounts for the isostatic rebound associated with erosion of overlying sediments on the northern side of the arch. Star marks contact of Miocene and Pliocene units along profile Line 2–2' from Fig. 1B, with pink box marking contact exposures within a swath extending  $\pm 40$  km from the profile. Black line is average topography for Line 2–2', calculated from the same swath. Light gray shading marks maximum and minimum values within swath. Dark gray shading marks area affected by significant post-Miocene faulting, which is not accounted for in our modeled uplift. A: Comparison of differing half-width (used to derive  $c$  parameter) values: orange line = 220 km, blue line = 210 km, red line (preferred value) = 200 km, green line = 190 km, black = 180 km. B: Comparison of differing maximum uplift ( $a$  parameter) values: orange line = 860 m of uplift, purple line = 810 m of uplift, blue line = 785 m of uplift, red line (preferred value) = 760 m of uplift, yellow line = 735 m of uplift, green line = 710 m of uplift, black line = 660 m of uplift. See text for discussion. (For interpretation of the references to color in this figure legend, the reader is referred to the web version of this article.)

We then discuss the results of these model calculations in Sections 4.1 and 4.2 respectively.

### 3.1. Gaussian approximation of rock uplift

Topographic uplift and associated erosion rapidly increase and then gradually decrease from northwest to southeast across the Fitzcarrald Arch (Espurt et al., 2010). The northwestern portion of the arch may have been obscured by earlier episodes of faulting and by post-Miocene erosion and deposition associated with the major Ucayali River system (Fig. 1). Because of this, we choose to model the arch's uplift along and parallel to the Andean mountain front as a 2-D Gaussian curve centered on the area of deepest structural exposure (Fig. 3). This profile has the advantage of lying in a swath where the most structural constraints are available, including a seismic reflection profile and two boreholes (Espurt et al., 2007a). In addition, the range parallel orientation removes the necessity of modeling the flexural subsidence effects of the mountain load. A Gaussian curve allows us to easily accommodate and characterize to a first-order the observed fall-off in rock uplift from northwest to southeast. While the volume of the arch could potentially

be modeled as a 3-D volume described by the rotation of a Gaussian curve, with a potentially varying inboard extent, the lack of published Miocene formation thicknesses in the eastern part of the arch prevents us from investigating this possibility. A 2-D Gaussian curve is defined by:

$$f(x) = a * \exp(-(x - b)^2 / (2 * c^2)). \quad (1)$$

The constant  $a$  is the highest value of the Gaussian's peak,  $b$  is the position of the peak relative to the origin of a Cartesian x-y grid, and  $c$  is the standard deviation of the Gaussian which controls the curve's width. As  $b$  is an arbitrary offset, Eq. (1) requires us to determine only parameters  $a$  and  $c$  to model the arch.

To determine parameters  $a$  and  $c$  we begin by examining the amount of uplift that has occurred in the Fitzcarrald Arch. In addition to the current topography, the uplift of the arch also includes a significant amount of eroded Miocene tidal deltaic and estuarine deposits (Espurt et al., 2010). Accounting for these yields a reference, pre-erosional Miocene surface that corresponds to the top of Espurt et al.'s (2010) Late Miocene Madre de Dios Formation.

We calculate the amount of uplift experienced by this Miocene surface by first finding the average topography for a cross-section striking approximately parallel to the Subandean thrust front and passing through the highest topographic expression of the Fitzcarrald Arch (profile 2–2', see Fig. 1B for location). Fig. 3 shows the averaged topographic swath for profile 2–2'. The thick black line in Fig. 3 marks the average topography of the arch found by averaging the Global Multi-Resolution Topography (GMRT) v.3.2 (Ryan et al., 2009) along 81 parallel profiles (profile 41 corresponds to 2–2' with additional profiles spaced at 1 km increments to a distance of +40 km/–40 km away from profile 2–2' to cover the current location of the arch's highest topography and minimize incorporation of Subandes topography into the swath); the gray region marks the maxima and minima of the topography encountered by these profiles.

We then marked the location where topographic profile 2–2' intersects the stratigraphic contacts between: 1) the Miocene Upper Ipururo—Miocene Lower Ipururo Formations (vertical red lines), 2) Upper Ipururo—Miocene Madre de Dios Formations (vertical orange line), and 3) Madre de Dios—Pliocene Juanjui/Corrientes Formations (red star) (Espurt et al., 2010). Exposure of these formations indicates that ~400 m of material from the Madre de Dios and ~300 m from the Upper Ipururo Formations above the Lower Ipururo has been eroded during the arch's formation (Espurt et al., 2010), and we use these values to find that the uplifted and eroded Miocene surface is at ~900 a.m.s.l. over the base of the Madre de Dios and at a maximum of ~1160 a.m.s.l. over the base of the Upper Ipururo (vertical dashed black lines in Fig. 3A). After correcting for isostatic rebound due to erosional unloading following the method of Molnar and England (1990), these values reduce to ~840 a.m.s.l. and ~970 a.m.s.l. respectively. Given the elevation of the surrounding basins is ~210 a.m.s.l., the maximum amount of uplift along this section of the Fitzcarrald Arch is ~760 m. We use these four formation contacts to provide the basis for our estimates of Gaussian parameters  $a$  and  $c$ .

Parameter  $c$  is relatively well constrained from the location of maximum uplift and the present exposure of the Madre de Dios Formation—Juanjui/Corrientes Formation contact along our topographic cross-section (red star in Fig. 3A). The mapped outcrop of the contact between these formations is highly irregular, indicating its surface exposure is largely dependent on the location of streams incising into the arch. The transparent pink box in Fig. 3A marks the approximate range of locations where streams near our cross-section have exposed the contact. We consider any value of parameter  $c$  that produces a Gaussian that intersects the average surface (black line) within this box to be a reasonable representation of the uplifted Miocene surface. The Gaussian curves shown in Fig. 3A have been calculated using the relationship:

$$c = w / (2 * \sqrt{2 * \ln 2}), \quad (2)$$

where  $w$  is the full width at half maximum or the distance at which the value of the Gaussian curve has decreased to one-half its maximum value. The values of  $w$  shown in Fig. 3A range from 360 km (black curve) to 440 km (orange curve), centered around our preferred value of 400 km (red curve) which passes directly through the outcrop of the contact along our cross-section (red star). As this value controls how rapidly the Gaussian defined by Eq. (1) decreases from its peak value but not the amplitude of this peak value, it has little effect on our calculation for the maximum amount of modification of the foreland necessary to uplift the Fitzcarrald Arch.

Parameter  $a$  in Eq. (1) describes the peak value of the Gaussian and is more important than  $c$  in modeling the amount of alteration necessary to create the arch. This parameter can be determined based on the arch's current topography and the amount of eroded Miocene material, ~760 m relative to the elevation of the surrounding basins. We recognize both that the uncertainty in the amount of eroded Miocene material and our assumption that removal of this material has been isostatically compensated may vary, and as a result have investigated the sensitivity of our uplift values. Fig. 3B shows values of parameter  $a$ , ranging from 660 m to 860 m, and their effects on the resulting Gaussian curves. All of these curves are consistent with outcrops of the Madre de Dios—Juanjui/Corrientes contact as their intersection with the land surface falls within the region where stream incision controls contact exposure (pink box in Fig. 3B); we consider the  $a = 660$  m Gaussian curve (black curve) a lower bound and the  $a = 860$  m Gaussian curve (orange curve) an upper bound for  $a$ .

In summary, we find that the Fitzcarrald Arch has ~760 m of associated rock uplift and can be characterized by a Gaussian half-width of ~200 km. Next, we evaluate potential causes of this uplift.

### 3.2. Quantitative models of arch uplift

As noted in Section 2, the uplift of the Fitzcarrald Arch may result from one of two isostatic mechanisms. The first mechanism, serpentinization of the base of the foreland mantle lithosphere, may be most easily modeled as a case of Pratt Isostasy in which the density of the lithosphere beneath the arch has been decreased relative to the surrounding basins. The second mechanism, crustal thickening at depth requires the use of Forsyth's (1985) equation for subsurface loading of an elastic plate.

#### 3.2.1. Uplift due to mantle lithosphere serpentinization

Partial serpentinization of the lithospheric mantle beneath the Fitzcarrald Arch would lower the average density of the lithospheric column beneath the arch, causing it to rise relative to its surroundings. The thickness of this column would be determined by the elastic thickness in the area (which may be interpreted as the depth of compensation for isostatic calculations) and the relationship between the present elevation of the arch and its initial elevation may be described by the Pratt equation for isostasy:

$$\rho_i * z = \rho_f (h + z) \quad (3)$$

with  $\rho_i$  representing the initial average density of the column,  $\rho_f$  representing its final average density following partial serpentinization of its mantle lithosphere component,  $z$  representing the thickness of the column, and  $h$  representing the elevation of the arch above its reference datum.

#### 3.2.2. Uplift through emplacement of material in the lower crust

Forsyth (1985) provides a method for the calculation of the amount of uplift produced by the emplacement of a load at depth within a plate that exploits multiplication in the spatial wave number ( $k$ ) domain to avoid the need to calculate fourth order derivatives in the spatial frequency domain (related to topography) simultaneously over a wide

range of spatial frequencies. This method relies on the equation:

$$W_b(k) = -\rho_c * H_b(k) * \phi / \Delta\rho, \quad (4)$$

where

$$\phi = 1 + (D * k^4) / (\rho_c * g). \quad (5)$$

In these equations, constants are limited to  $\rho_c$  (crustal density),  $\Delta\rho$  (difference between mantle and crustal densities),  $g$  (gravitational acceleration), and  $D$  (flexural rigidity). The constant  $D$  is defined in relation to the material parameters of the plate  $E$  (its Young's modulus),  $T_e$  (its elastic thickness) and  $\nu$  (its Poisson's ratio) through the equation:

$$D = (E * T_e^3) / [12 * (1 - \nu^2)]. \quad (6)$$

The variable  $k$  (spatial wave number) in Eqs. (4) and (5) defines both functions  $W_b(k)$  (the Fourier transform of the amplitude of Moho deflection from some reference depth) and  $H_b(k)$  (the Fourier transform of topography).

For our investigation of the Fitzcarrald Arch only a single value of  $k$  (here interpreted as the spatial wavelength of rock uplift related to the arch's areal extent) is of interest. This further simplifies Eqs. (4) and (5) by rendering the term  $D * k^4$  in Eq. (5) a constant. Observing the linearity property of Fourier transforms we find that:

$$\square^{-1}(W_b(k)) = \square^{-1}(-\rho_c * H_b(k) * \phi / \Delta\rho) = -\rho_c * \phi / \Delta\rho * \square^{-1}(H_b(k)). \quad (7)$$

This makes Eq. (4) equivalent to:

$$W_b(x) = -\rho_c * \phi / \Delta\rho * H_b(x), \quad (8)$$

further simplifying calculation.  $W_b(x)$  is the downward deflection of the Moho resulting from the addition of material given an observed topographic uplift of  $H_b(x)$ . In our case,  $H_b(x)$  is the Gaussian function defined above and the term  $-\rho_c * \phi / \Delta\rho$  acts to scale the peak amplitude of this Gaussian (the Gaussian parameter  $a$  discussed above). We investigate the relationship between this scaling factor and physical parameters below.

## 4. Results

### 4.1. Mantle serpentinization models

Following Sacek and Ussami's (2009) evaluation utilizing geologic and geophysical observations of existing elastic thickness models for South America, we use the best fit value of 50 km for our study region's elastic thickness (Stewart and Watts, 1997) and assign  $h$  our preferred value of arch uplift, 760 m. We then find that the ratio  $\rho_i/\rho_f$  equals 1.015. Assuming that the crust is 35 km thick and has a density of 2670 kg/m<sup>3</sup> and that the un-serpentinized mantle had a density of 3300 kg/m<sup>3</sup> we find that the average density of the initial column would be 2860 kg/m<sup>3</sup> and further that the density of the partially serpentinized mantle lithosphere would be 3170 kg/m<sup>3</sup> (a density change of ~4%). This value corresponds to ~20% by volume antigorite in the lithospheric mantle and a shear wave velocity of ~4.4 km/s (Abers and Hacker, 2016). Assuming the lowest estimate of arch uplift consistent with geological data, 660 m, yields an equivalent value while assuming a significantly thicker elastic thickness (70 km), yields partially serpentinized lithospheric mantle with a density of 3230 kg/m<sup>3</sup>. This value corresponds to ~10% by volume antigorite and a shear wave velocity of ~4.5 km/s (Abers and Hacker, 2016). Halving the elastic thickness would result in a thickness less than our crustal thickness, meaning that the depth of isostatic compensation would occur predominately within the crust. This would largely decouple surface uplift from processes within the mantle like serpentinization. Surface (shear) wave tomography results (Antonijevic et al., 2015) for the region do not have sufficient resolution to test these predictions. However, there are three prior observations that suggest that the slab dehydrates several hundred kilometers west of the arch and is not dehydrating under the arch itself (see Hasegawa and Nakajima, 2017 for review of the general

relationships between seismic observations and slab dehydration): 1) the lack of earthquakes in the slab beneath the arch (Kumar et al., 2016, see also Fig. 2); 2) high seismic velocities in the slab's crust well west of the arch (Bishop et al., 2017, see Fig. 2) suggesting the oceanic crust has transformed to relatively anhydrous eclogite; and 3) the presence of a thin supra-slab mantle hydration layer, associated with water released from the dehydrating slab (Dougherty and Clayton, 2015), that disappears well to the west of the arch. This suggests that hydration of the mantle is an unlikely source of arch uplift and an alternate model of arch uplift is necessary.

#### 4.2. Crustal thickening models

Calculation of the amount of uplift produced by the emplacement of a load at depth within a plate requires a total of six independent physical parameters (see Eq. (6) in Section 3.2.2.), three of which (Young's modulus ( $E$ ), elastic thickness ( $T_e$ ), and Poisson's ratio ( $\nu$ )) are necessary to calculate the flexural rigidity parameter,  $D$ . We begin by assigning these parameters based upon prior studies of the Andean foreland and our Gaussian approximation of the rock uplift associated with the Fitzcarrald Arch. We then use alternate, geologically reasonable values of these parameters to examine how departures from these regional observation-based values may affect our estimate of crustal thickening beneath the Fitzcarrald Arch (see Fig. 4).

We again use Stewart and Watts's (1997) parameters for the region around the arch ( $E = 1 \times 10^{11}$  Nm,  $\nu = 0.25$ ,  $g = 9.81$  m/s<sup>2</sup>,

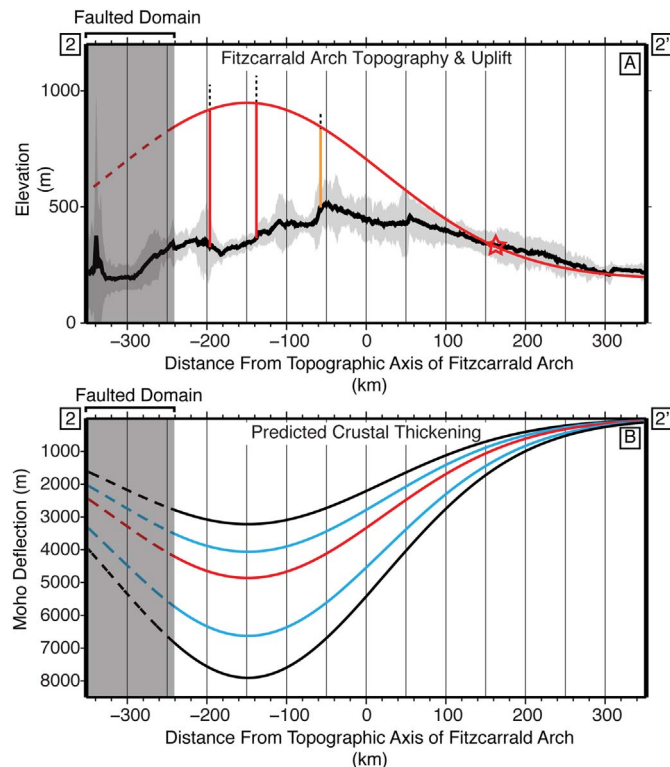


Fig. 4. A: Miocene surface (red curve) uplifted during formation of the Fitzcarrald Arch calculated from surface exposures of Miocene contacts and corresponding erosion documented by Espurt et al. (2010) (topography and other features as in Fig. 3). B: Calculated amount of crustal material needed to support the uplift in A assuming range of differing plate properties. Red line marks our preferred model (4.9 km maximum thickening), blue lines mark range of values obtained from alternate models (see Table 1, range extends from ~4 to 6.6 km of maximum thickening). Black lines mark extreme values, with shallowest (~3.2 km of maximum thickening) corresponding to pure Airy isostatic support for the arch and the deepest (~7.9 km of maximum thickening) corresponding to extreme values of mantle and crustal densities (3200 kg/m<sup>3</sup> and 2800 kg/m<sup>3</sup> respectively). See text for discussion. (For interpretation of the references to color in this figure legend, the reader is referred to the web version of this article.)

Table 1  
Sensitivity analysis for thickening estimate.

Parameter	Assumed value	Resultant thickening (km)
Elastic thickness (km)	25	3.4
Elastic thickness (km)	40	4.1
Elastic thickness (km)	60	6.1
Young's modulus (Pa*s)	$2.0 \times 10^{11}$	6.5
Young's modulus (Pa*s)	$5.0 \times 10^{10}$	4.0
Poisson's ratio	0.2	4.8
Poisson's ratio	0.3	4.9
Topographic wave number (km <sup>-1</sup> )	$2 * \pi / 500$	6.6
Topographic wave number (km <sup>-1</sup> )	$2 * \pi / 700$	4.1
Crustal, mantle density (kg/m <sup>3</sup> )	2670, 3200	5.8
Crustal, mantle density (kg/m <sup>3</sup> )	2670, 3400	4.2
Crustal, mantle density (kg/m <sup>3</sup> )	2700, 3200	6.2
Crustal, mantle density (kg/m <sup>3</sup> )	2700, 3300	5.1
Crustal, mantle density (kg/m <sup>3</sup> )	2700, 3400	4.4
Crustal, mantle density (kg/m <sup>3</sup> )	2800, 3200	7.9
Crustal, mantle density (kg/m <sup>3</sup> )	2800, 3300	6.3
Crustal, mantle density (kg/m <sup>3</sup> )	2800, 3400	5.3

$\rho_c = 2670$  kg/m<sup>3</sup>,  $\rho_m = 3300$  kg/m<sup>3</sup>,  $T_e = 50$  km) and assign  $k$  and derive  $H_b(x)$  values from the topographic expression of the arch (~600 km) and our estimate for the uplifted Miocene surface (~760 m at apex relative to neighboring basins, full width at half-maximum ~200 km). These values result in ~4.9 km of crustal thickening beneath the maximum observed uplift (Fig. 4B). We treat this result as a reference value and now examine the effects of alternating the values of our model parameters (see Table 1). We first examine the three parameters that define  $D$ , the plate's flexural rigidity.

Our preferred value of  $E$  ( $1 \times 10^{11}$  Nm) is fairly typical for crustal materials. Lithospheric mantle values may reach nearly double this value (Tesauro et al., 2012). Likewise, while  $\nu$  is on average around 0.25, varying compositions and pressure/temperature conditions may cause  $\nu$  to vary by approximately  $\pm 0.05$  (Christensen, 1996). Table 1 shows that varying the value of  $E$  by  $\times 0.5$  or  $\times 2$  has an effect comparable to modifying the value of  $T_e$  by  $\pm 10$  km. Alternatively, halving  $T_e$  to a value of 25 km yields 3.4 km of crustal thickening. Varying the value of  $\nu$  has no significant effect. This indicates that variation in  $D$  may change our estimated value of crustal thickening by ~1 to 1.5 km yielding a range of potential thickening values from ~4 km to 6.5 km.

Comparable ranges of estimated crustal thickening values are obtained by variation in the spatial wave number,  $k$  (equivalent to  $2\pi$ /spatial wavelength). The topographic expression of most of the Fitzcarrald Arch is clear in the Global Multi-Resolution Topography data set (Ryan et al., 2009), however the low amplitude flanks of the arch may be partially obscured by the topography of the Subandean foothills. To investigate potential errors in determining the spatial wavelength of the arch, we test wavelengths of  $\pm 100$  km differences from our estimate of 600 km. We find that a 500 km wavelength would require 6.6 km of crustal thickening to account for the Arch's uplift and a 700 km wavelength would require 4.1 km of thickening.

The final parameters that may affect our calculation are the average densities of the crust and mantle lithosphere beneath the Fitzcarrald Arch. As our calculation depends on the difference between the crust and mantle density, we report pairs of values in Table 1. We find that most combinations of crust and mantle densities yield thickening estimates in the same range (~4 to 6.5 km) as the other parameters we examined above, however in an extreme case with high-density crust (2800 kg/m<sup>3</sup>) and unusually low-density mantle (3200 kg/m<sup>3</sup>) requires 7.9 km of thickening to produce the arch.

The above investigation of parameters suggests that a minimum of ~4 km of thickening is likely to have occurred to support the uplift of the Fitzcarrald Arch, and suggests that our preferred value of ~4.9 km is reasonable. The values calculated for all parameters are noticeably different from the value of 3.2 km of thickening required to support the arch's uplift assuming local Airy isostasy (equivalent to setting the

flexural rigidity parameter  $D$  or elastic thickness parameter  $T_e$  to 0). Improved seismic coverage of the arch and neighboring basins may be able to distinguish between the Airy isostatic estimate and a number of the flexurally supported estimates. Flexural estimates of thickening based on the range of geologically reasonable values that we have examined are comparable in magnitude to the localized  $\sim 5$  km thickening observed southeast of subducted Nazca Ridge beneath the high Andean Cordillera (Bishop et al., 2017), suggesting that similar processes may have been responsible for thickening both locations.

## 5. Discussion

### 5.1. Thickening foreland lower crust with minimal upper crustal faulting

We propose that the uplift of the Fitzcarrald Arch was likely driven by  $\sim 4$  km to 6.5 km of crustal thickening beneath the arch, and given that the arch lacks significant post-Cretaceous faulting and crustal seismicity (Espurt et al., 2007a, 2007b) this thickening would need to be accommodated ductilely. This thickening is consistent with Regard et al.'s (2009) suggestion that the arch is a product of increased coupling between the flat slab and the overriding plate. However, the extension of the Fitzcarrald Arch beyond the point at which the flat slab resteepests (see Fig. 2) raises a further question: how can a flat slab trigger significant thickening of the overriding plate's lower crust beyond the slab's subduction hinge without corresponding faulting in the upper crust?

Numerical modeling of a shallowly subducting plate mechanically coupled to an overriding plate may provide an explanation. Bird (1988) has shown that basal shear can displace a volume of material sufficient to thin the overriding plate's crust by up to  $> 20$  km near the trench and to thicken it by up to  $> 20$  km where the subducting plate steepens and decouples from the overriding plate. Changes in lithospheric mantle thickness follow a similar, though more extreme, pattern (Bird, 1988). This thickening may extend beyond the point of decoupling, decreasing with distance beyond the slab hinge (Bird, 1984). Absolute magnitudes of thickening and thinning vary based on the rheology of the overriding plate as well as on the extent of coupling between the two plates, but significant shear strain is likely to accumulate in the lower crust of the overriding plate (Bird, 1984). In locations where the flat slab extends to the foreland and where the subducting and overriding plates are partially coupled, Bird's (1984, 1988) models predict both crustal thickening and associated topographic uplift. This model differs from channel flow models of crustal thickening (see Jamieson and Beaumont, 2013 for a review of channel flow) in maintaining coupling between the ductilely deforming layer of crust and a stronger underlying lower crust or mantle lithosphere, imparting a single top-towards-the-trench sense of shear to the deforming layer (Bird, 1984; Allmendinger and Judge, 2014).

Observations of the forearc and high Andes above the subducted Nazca Ridge along the southern edge of the Peruvian flat slab are largely consistent with the deep crust and mantle structure predictions of Bird's models. While variations in the crust and lithospheric mantle thickness prior to flat subduction have likely lead to greater heterogeneity than modeled by Bird (1984, 1988) with a uniform upper plate, these simple models are a good first-order match for the Fitzcarrald Arch region. Extensive removal of the South American lithospheric mantle along the inboard projection of the Nazca Ridge (Bishop et al., 2017; Eakin et al., 2014b) and thinning of South American crust above the subducted Nazca Ridge (Bishop et al., 2017) is consistent with the basal shear models' thinning predictions in the overriding plate where the plate and flat slab along the Nazca Ridge are coupled. Evidence for thickening of the Andean crust by  $\sim 5$  km inboard of the southeast edge of the flat slab (Bishop et al., 2017) is consistent with the models' prediction for crustal thickening in the direction of convergence immediately beyond the region of interplate coupling.

A lack of seismic array coverage in the foreland prevents direct

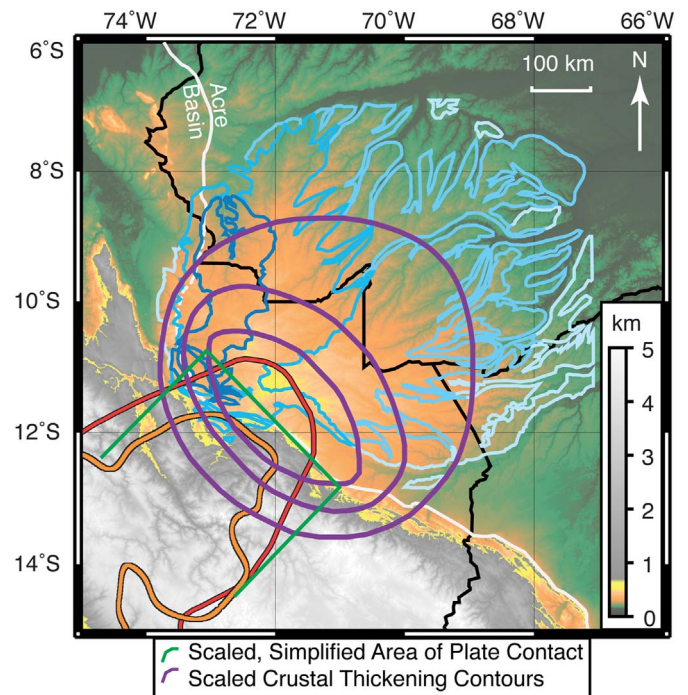


Fig. 5. Topographic and geologic expression of the Fitzcarrald Arch (as in Fig. 1B) compared to Bird's (1984) basal shear model scaled approximately to the Nazca plate's subducted oceanic Moho 80 km depth contour (Bishop et al., 2017) and the Nazca plate's 90 km surface wave tomographic depth contour (Antonijevic et al., 2015). Note that as shown in Fig. 2 the irregularities in the 80 km slab Moho contour along the eastern edge occur in an area where the slab remains in close contact with the overriding continental crust. Green line show the area of plate contact scaled from Bird (1984) to match slab contours; purple lines show qualitative crustal thickening contours caused by basal shear scaled from Bird (1984). See text for discussion. (For interpretation of the references to color in this figure legend, the reader is referred to the web version of this article.)

observation of the South American continental Moho beneath the Fitzcarrald Arch, preventing us from directly investigating the crustal thickness beneath the arch. Array coverage does allow examination of the crustal thickness at the Subandean deformation front, where crustal thickness range between  $\sim 50$  and 55 km (Bishop et al., 2017; see Fig. 2). Immediately north of the Fitzcarrald Arch James and Snoke (1994) found that the crustal thickness at Subandean deformation front ranged between  $\sim 40$  and 45 km while south of the arch Ryan et al. (2016) likewise found crustal thickness of  $\sim 40$ –45 km at the deformation front. These observations are consistent with our model's predictions of  $> 5$  km of crustal thickening beneath the arch. In addition, by scaling Bird's (1984) model to a point between 80 km and 90 km depth contour for the slab's subducted oceanic Moho from Bishop et al. (2017) and Antonijevic et al. (2015), we can compare the topographic expression of the arch and the potential area of basal shear induced crustal thickening caused by the subducted ridge (Fig. 5). Bird's (1984) model is dimensionless, so its contours represent qualitative estimates of an instantaneous crustal thickening rate (which depends on the strength of the overriding plate and magnitude of basal shear stress, the values of which are both presently unknown) rather than total crustal thickening. As such it only allows us to determine whether the potential "footprint" of deformation has a location and geometry that is consistent with the arch. While complications seem to exist on the south-eastern edge of the flat slab, Fig. 5 highlights how the "footprint" of active crustal thickening predicted by the coupling model is a good match for the region of high topography associated with the arch. A comparison of topography and exposed Miocene sedimentary units suggests there is a discordance between the areas of highest topography and highest structural exhumation. This discordance appears to the northeast of predicted high present rates of crustal

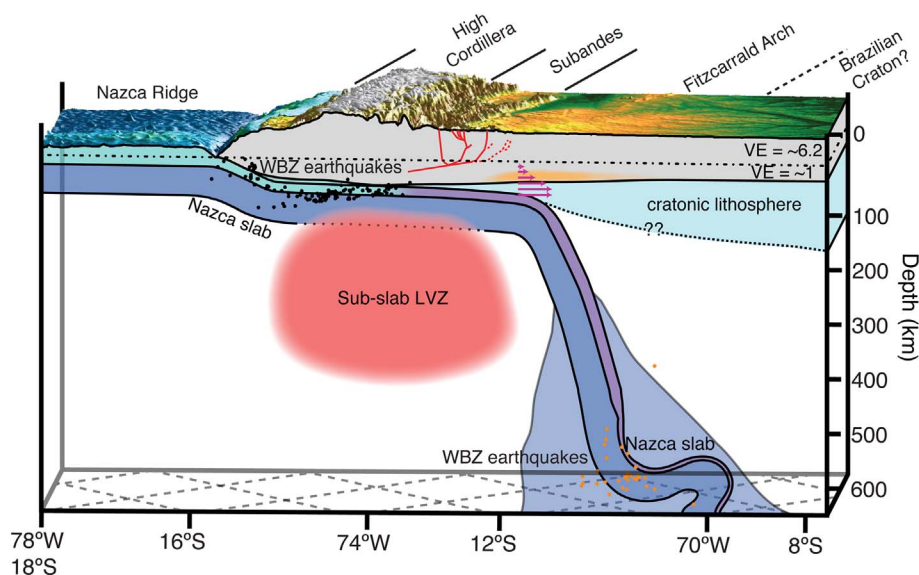


Fig. 6. Schematic cross-section approximately following strike of the subducting Nazca Ridge. Solid black lines above topography mark boundaries between geomorphic features, dashed black line marks inferred location of the edge of the stable Brazilian Craton. Light blue on subducting Nazca plate and slab represents basaltic crust, purple represents eclogitized crust associated with end of intermediate depth Wadati-Benioff zone seismicity (black circles representing hypocenters from Kumar et al. (2016)  $\pm 150$  km from cross-section, see Fig. 2 above for discussion of eclogitization). Dark blue represents oceanic mantle lithosphere, with broadening slab velocity anomaly in the mantle transition zone (Scire et al., 2017) and deep seismicity (International Seismological Center, 2011) interpreted as representing deformation of the slab as it begins to enter the lower mantle. Red feature below the slab represents potentially buoyant low seismic velocity feature (Antonijevic et al., 2015; Scire et al., 2016) beneath the flat slab. Within the crust of the over-riding South American plate (gray, note change in vertical exaggeration at 8 km depth to accommodate topography/bathymetry), solid red lines mark the location of active (reactivated?) Subandean thrust faults while dashed red lines mark inactive pre-Cretaceous faults (following Devlin et al., 2012) while area in orange marks the approximate location of mid-to-lower crustal thickening we predict to drive the uplift of the Fitzcarrald Arch. Purple arrows provide sense of motion for the region of crustal thickening beneath the Fitzcarrald Arch; note that this motion would impart a top-to-the-west sense of shear to the ductilely deforming mid-to-lower crust, opposite to the overall top-to-the-east sense of shear caused by Subandean thrust-faulting in the neighboring upper crust. The thickness of the cratonic lithosphere (light blue beneath overriding plate) is uncertain, however gradually increasing elastic thicknesses towards the east (see Sacek and Ussami, 2009 for compilation) suggest it may be somewhat tapered, with an increasing thickness towards the east. See text for discussion. (For interpretation of the references to color in this figure legend, the reader is referred to the web version of this article.)

thickening—consistent with southeastward propagation of the arch through time as the Nazca Ridge migrates with respect to stable South America (Espurt et al., 2007a, 2010).

## 5.2. Broader implications

We show in Fig. 6 our schematic cross-section of the southern segment of the Peru flat slab where the Nazca Ridge is subducting and the proposed basal shear that could account for the uplift of the Fitzcarrald Arch. The development of the Fitzcarrald Arch through thickening of the lower crust represents one of the most spatially extensive examples of crustal thickening due to flat slab induced basal shear. This mechanism is structurally quite different from the basement cored uplifts attributed to basal shear associated with other flat slab regions (e.g. Dickinson and Snyder, 1978; Jordan and Allmendinger, 1986; and see Erslev, 2005 for a critical review). The lack of significant faulting within the  $\sim 2.5$  km thick Cretaceous to late Cenozoic sedimentary layers (Espurt et al., 2010) or of reactivation of pre-Cretaceous basement faults present on the arch (Gautheron et al., 2013) indicates that thickening must be accommodated in the mid-to-lower crust. This contrasts with both basement cored uplifts and other occurrences of shallow crustal faulting observed in other flat slab localities, including the northern segment of the Peruvian flat slab (Hermoza et al., 2006; Eude et al., 2015; see Figs. 1 and 5). The differences in deformation style in the upper plate above the same flat slab may reflect structural (e.g. orientation of pre-existing faults (Gautheron et al., 2013)) or rheological differences (e.g. variations in the relative strength of the lower crust and mantle lithosphere) between the Fitzcarrald Arch and the region immediately to the north and west. In addition, the differences between the two regions may reflect differences in the structure of the flat slab. The flat slab around the subducted Nazca Ridge is significantly shallower than the region immediately northwest of the ridge (Gutscher et al., 1999). Although the Nazca Ridge began to enter the trench near  $\sim 10^\circ\text{S}$  around 15–11 Ma (Hampel, 2002; Rosenbaum et al., 2005), the volcanic arc remained active between  $\sim 10^\circ\text{S}$  and  $\sim 14^\circ\text{S}$  until 4 Ma (Rosenbaum et al., 2005). This delay is consistent with analogue and numerical models (Espurt et al., 2008; Hu et al., 2016) that find several million years elapse between initial ridge subduction and full flattening of the slab and with the approximate timing

of the Fitzcarrald Arch's uplift (Espurt et al., 2010). Prior to flattening and the closure of the convecting mantle wedge, the slab and overriding plate would be largely uncoupled, preventing basal shear above and inboard of the ridge. This possibility does not explain why the shallow northern segment of the Peruvian flat slab, associated with the hypothesized subducted Inca Plateau (Gutscher et al., 1999), has failed to form a comparable arch-like feature near  $5^\circ\text{S}$ . Further geological and geophysical investigation of the region may help to clarify the evolution of the Peruvian flat slab and the conditions necessary for the formation of foreland arches and basement cored uplifts.

The differences in foreland deformation style between the southern segment of the Peruvian flat slab associated with the subducted Nazca Ridge and the northern segment highlight the variability in responses to ridge subduction. This variability is further highlighted when examining the subduction of other ridges in South America (see Gutscher et al., 2000 and Spikings and Simpson, 2014 for overviews). While both the Nazca Ridge and Juan Fernandez Ridge (Allmendinger and Judge, 2014) show evidence for basal shear, there are major differences between the two. At a depth of  $\sim 100$ – $110$  km, the Pampean flat slab associated with the subducting Juan Fernandez Ridge is deeper than that associated with the Nazca Ridge and a significant thickness of mantle lithosphere is present between the continental crust and the Pampean flat slab (Gans et al., 2011). In addition, crustal deformation is accommodated by basement cored uplifts and abundant deep crustal earthquakes above the eastern portion of the Pampean flat slab and east of where the flat slab re-steepens (e.g. Alvarado et al., 2009; Bellahsen et al., 2016). The subducting Juan Fernandez Ridge associated with the shallowest portion of the Pampean flat slab thus appears to show both ductile crustal thickening beneath the western Precordillera fold belt and basement cored faulting to the east in the Sierras Pampeanas region.

There is little evidence for significant basal shear occurring within the Andean foreland inboard of the subducting Carnegie and Iquique Ridges. We note that at both locations the volcanic arc remains active (though broadened near the Carnegie Ridge) (Gutscher et al., 2000). This indicates that in these locations the subducting and overriding plates likely remain decoupled by an intervening mantle wedge, and hence would not be expected to cause any basal shear. Perhaps the subducting Carnegie and Iquique Ridges have either just begun to

subduct or have otherwise not had time to cause the associated slab to become flat, consistent with models that find a delay between the initial subduction of a buoyant feature and the establishment of flat slab geometry (e.g. [Espurt et al., 2008](#); [Hu et al., 2016](#)). Comparison of these four ridges indicates: (1) that the onset of ridge subduction may not immediately produce a response in the overriding plate, other than offshore and near the coast; and (2) the upper plate may respond through variable styles of deformation, both within a single flat slab system and between separate flat slab segments along the same subduction zone.

In light of the observations we have presented above and recent evidence for flat slab related basal shear induced thickening in the Argentine Precordillera above the Sierras Pampeanas flat slab ([Allmendinger and Judge, 2014](#)), it may be useful to reconsider the importance and expression of flat slab induced basal shear in the evolution of Cordilleran mountain belts. [Bird's \(1984, 1988\)](#) model of basal shear thickening was originally developed as an explanation for flat slab related Laramide structures in western North America and the continued presence of a thick continental mantle lithosphere in the region has been difficult to explain (see [Erslev, 2005](#) and references therein). Both our observations of the Fitzcarrald Arch and observations of basal shear induced thickening of the Argentine Precordillera above the shallow portion of Pampean flat slab ([Allmendinger and Judge, 2014](#)) suggest that the effects of basal shear may be concentrated over the shallowest portions of a flat slab. In these two cases, the evidence for basal shear corresponds with the location of subducting aseismic ridges or hot spot tracks and associated sub-slab low velocity bodies in both Peru ([Antonijevic et al., 2015](#); [Scire et al., 2016](#)) and Argentina ([Anderson et al., 2007](#); [Portner et al., 2017](#)) rather than over the entirety of a flat slab region.

Recent geological observations from western North America may be consistent with this localized form of basal shear. Subduction complex-derived schists emplaced at mid-to-lower crustal depths in western Arizona ([Haxel et al., 2015](#)) lie along the center of the proposed Laramide flat slab and the predicted path of the subducted oceanic plateau associated with the formation of this flat slab ([Liu et al., 2010](#)). Extensive Laramide age shearing observed in mantle xenoliths found near the center of the Colorado Plateau ([Behr and Smith, 2016](#)) are also located above the path of the subducted oceanic plateau. We suggest basal shear deformation in the Laramide flat slab may have been concentrated—and therefore most disruptive of the overriding plate's lithosphere—directly above the central portion of the subducting Laramide oceanic plateau, just as observed in the modern Peruvian flat slab and in the Pampean flat slab ([Allmendinger and Judge, 2014](#)).

The concentration of deformation in the upper plate directly above subducting aseismic ridges or oceanic plateaus may explain the contradiction between the general preservation of the western North American continental lithosphere and the evidence of severe local disruption of the continental lithosphere represented by these schist and mantle xenoliths. Analogous to Peru and Argentina, outside of a relatively narrow corridor directly over the subducted plateau, disruption is likely to have been limited. Other less extensively documented occurrences of flat subduction in the geologic record (e.g. the compilation by [Ramos and Folguera \(2009\)](#) for examples from South America) may exhibit similar patterns of deformation as further details of these occurrences are uncovered.

## 6. Conclusions

We illustrate an overall view of the relationship between the Fitzcarrald Arch and the subducting flat slab in Peru ([Fig. 6](#)). The formation of the Fitzcarrald Arch in the foreland of the Andes occurs along the projection of the subducted Nazca Ridge. We suggest that the Fitzcarrald Arch is the result of thickening on the order of ~5 km in the foreland's mid-to-lower crust as the result of top-to-the-west basal shear and shortening between the shallowest portion of the flat slab,

coincident with the subducted Nazca Ridge, and the South American lithosphere. A lack of seismicity and surface faulting associated with the Fitzcarrald Arch indicates that this basal shear and shortening is accommodated ductilely in the mid-to-lower crust and dissipates before significantly affecting the brittle upper crust. This process suggests that basal shear induced deformation in the overriding plate in a flat slab setting is concentrated along only the shallowest segment of the flat slab. In Peru, this corresponds to the shallow subducted Nazca Ridge, and elsewhere is likely to correspond to other shallow subducted aseismic ridges or oceanic plateaus. Other styles of upper plate deformation may be important when the flat slab segments are deeper.

## Acknowledgements

This work was supported by NSF grants EAR-0943991, EAR-1415914, EAR-0943962, EAR-0944184. B. Bishop was also supported by: UA Graduate College Scholarship and a ChevronTexaco Geology Fellowship. We also thank Rob Govers, Nicolas Espurt, and an anonymous reviewer for their comments and suggestions that have greatly aided us in improving this manuscript.

## References

- Abers, G.A., Hacker, B.R., 2016. A MATLAB toolbox and Excel workbook for calculating the densities, seismic wave speeds, and major element composition of minerals and rocks at pressure and temperature. *Geochem. Geophys. Geosyst.* 17, 616–624. <http://dx.doi.org/10.1002/2015GC006171>.
- Allmendinger, R.W., Judge, P.A., 2014. The Argentine Precordillera: a foreland thrust belt proximal to the subducted plate. *Geosphere* 10 (6), 1203–1218. <http://dx.doi.org/10.1130/GES01062.1>.
- Alvarado, P., Pardo, M., Gilbert, H., Miranda, S., Anderson, M., Saez, M., Beck, S., 2009. Flat-slab subduction and crustal models for the seismically active Sierras Pampeanas region of Argentina. In: Kay, S.M., Ramos, V.A., Dickinson, W.R. (Eds.), *Backbone of the Americas: Shallow Subduction, Plateau Uplift and Ridge and Terrane Collision*. Geological Society of America Memoir, vol. 204. pp. 261–278. [http://dx.doi.org/10.1130/2009.1204\(12\)](http://dx.doi.org/10.1130/2009.1204(12)).
- Ammirati, J.-B., Alvarado, P., Beck, S., 2015. A lithospheric velocity model for the flat slab region of Argentina from joint inversion of Rayleigh wave phase velocity dispersion and teleseismic receiver functions. *Geophys. J. Int.* 202, 224–241. <http://dx.doi.org/10.1093/gji/ggv140>.
- Anderson, M., Alvarado, P., Zandt, G., Beck, S., 2007. Geometry and brittle deformation of the subducting Nazca Plate, central Chile and Argentina. *Geophys. J. Int.* 171, 419–434. <http://dx.doi.org/10.1111/j.1365-246X.2007.03483.x>.
- Antonijevic, S.K., Wagner, L.S., Kumar, A., Beck, S.L., Long, M.D., Zandt, G., Tavera, H., Condori, C., 2015. The role of ridges in the formation and longevity of flat slabs. *Nature* 524, 212–215. <http://dx.doi.org/10.1038/nature14648>.
- Antonijevic, S.K., Wagner, L.S., Beck, S.L., Long, M.D., Zandt, G., Tavera, H., 2016. Effects of change in slab geometry on the mantle flow and slab fabric in Southern Peru. *J. Geophys. Res.* 121, 7252–7270. <http://dx.doi.org/10.1002/2016JB013064>.
- Arrial, P.-A., Billen, M.I., 2013. Influence of geometry and eclogitization on oceanic plateau subduction. *Earth Planet. Sci. Lett.* 363, 34–43. <http://dx.doi.org/10.1016/j.epsl.2012.12.011>.
- Barazangi, M., Isacks, B.L., 1976. Spatial distribution of earthquakes and subduction of the Nazca plate beneath South America. *Geology* 4 (11), 686–692. [http://dx.doi.org/10.1130/0091-7613\(1976\)4<686:SDOEAS>2.0.CO;2](http://dx.doi.org/10.1130/0091-7613(1976)4<686:SDOEAS>2.0.CO;2).
- Behr, W.M., Smith, D., 2016. Deformation in the mantle wedge associated with Laramide flat-slab subduction. *Geochem. Geophys. Geosyst.* 17, 2643–2660. <http://dx.doi.org/10.1002/2016GC006361>.
- Bellahsen, N., Sebrier, M., Siame, L., 2016. Crustal shortening at the Sierra Pie de Palo (Sierras Pampeanas, Argentina): near-surface basement folding and thrusting. *Geol. Mag.* 153, 992–1012. <http://dx.doi.org/10.1017/S0016756816000467>.
- Bird, P., 1984. Laramide crustal thickening event in the Rocky Mountain Foreland and Great Plains. *Tectonics* 3, 741–758. <http://dx.doi.org/10.1029/T0003i007p00741>.
- Bird, P., 1988. Formation of the Rocky Mountains, western United States: a continuum computer model. *Science* 239, 1501–1507. <http://dx.doi.org/10.1126/science.239.4847.1501>.
- Bishop, B.T., Beck, S.L., Zandt, G., Wagner, L., Long, M., Antonijevic, S.K., Kumar, A., Tavera, H., 2017. Causes and consequences of flat slab subduction in southern Peru. *Geosphere* 13 (5), 1392–1407. <http://dx.doi.org/10.1130/GES01440.1>.
- Bump, A., 2003. Reactivation, trishear modelling, and folded basement in Laramide uplifts: implications for the origins of intra-continental faults. *GSA Today* 13 (3), 4–10. [http://dx.doi.org/10.1130/1052-5173\(2003\)013<004:RTMAFB>2.0.CO;2](http://dx.doi.org/10.1130/1052-5173(2003)013<004:RTMAFB>2.0.CO;2).
- Christensen, N.I., 1996. Poisson's ratio and crustal seismology. *J. Geophys. Res.* 101 (B2), 3139–3156. <http://dx.doi.org/10.1029/95JB03446>.
- Currie, C.A., Beaumont, C., 2011. Are diamond-bearing Cretaceous kimberlites related to low-angle subduction beneath western North America? *Earth Planet. Sci. Lett.* 303, 59–70. <http://dx.doi.org/10.1016/j.epsl.2010.12.036>.
- Dávila, F.M., Lithgow-Bertelloni, C., 2015. Dynamic uplift during slab flattening. *Earth Planet. Sci. Lett.* 425, 34–43. <http://dx.doi.org/10.1016/j.epsl.2015.05.026>.

- Devlin, S., Isacks, B.L., Pritchard, M.E., Barnhart, W.D., Lohman, R.B., 2012. Depths and focal mechanisms of crustal earthquakes in the central Andes determined from teleseismic wave-form analysis and InSAR. *Tectonics* 31, TC2002. <http://dx.doi.org/10.1029/2011TC002914>.
- Dickinson, W.R., Snyder, W.S., 1978. Plate tectonics of the Laramide orogeny. In: Mathews IIIV. (Ed.), *Laramide Folding Associated With Basement Block Faulting in the Western United States*. Geological Society of America Memoir, vol. 151. pp. 355–366. <http://dx.doi.org/10.1130/MEM151-p355>.
- Dougherty, S.L., Clayton, R.W., 2015. Seismic structure in southern Peru: evidence for a smooth contortion between flat and normal subduction of the Nazca Plate. *Geophys. J. Int.* 200, 534–555. <http://dx.doi.org/10.1093/gji/ggu415>.
- Dumont, J.F., Deza, E., García, F., 1991. Morphostructural provinces and neotectonics in the Amazonian lowlands of Peru. *J. S. Am. Earth Sci.* 4, 373–381. [http://dx.doi.org/10.1016/0895-9811\(91\)90008-9](http://dx.doi.org/10.1016/0895-9811(91)90008-9).
- Eakin, C.M., Lithgow-Bertelloni, C., Dávila, F.M., 2014a. Influence of Peruvian flat-subduction on the evolution of western Amazonia. *Earth Planet. Sci. Lett.* 404, 250–260. <http://dx.doi.org/10.1016/j.epsl.2014.07.027>.
- Eakin, C.M., Long, M.D., Beck, S.L., Wagner, L.S., Tavera, H., Condori, C., 2014b. Response of the mantle to flat slab evolution: insights from local S splitting beneath Peru. *Geophys. Res. Lett.* 41, 3438–3446. <http://dx.doi.org/10.1002/2014GL059943>.
- Erslev, E.A., 2005. 2D Laramide geometries and kinematics of the Rock Mountains, western U.S.A. In: Kalstrom, K.E., Keller, G.R. (Eds.), *The Rocky Mountain Region: An Evolving Lithosphere Tectonics, Geochemistry, and Geophysics*. American Geophysical Union, Washington, D.C., U.S.A., pp. 7–20. <http://dx.doi.org/10.1029/154GM02>.
- Espurt, N., Baby, P., Brusset, S., Roddaz, M., Hermoza, W., Regard, V., Antoine, P.O., Salas-Gismondi, R., Bolaños, R., 2007a. How does the Nazca Ridge subduction influence the modern Amazonian foreland basin? *Geology* 35 (6), 515–518. <http://dx.doi.org/10.1130/G23237A.1>.
- Espurt, N., Baby, P., Brusset, S., Roddaz, M., Hermoza, W., Regard, V., Antoine, P.O., Salas-Gismondi, R., Bolaños, R., 2007b. How does the Nazca Ridge subduction influence the modern Amazonian foreland basin?: reply. *Geology* 35, e163. <http://dx.doi.org/10.1130/G24631Y.1>.
- Espurt, N., Funicello, F., Martinot, J., Guillaume, B., Regard, V., Faccenna, C., Brusset, S., 2008. Flat subduction dynamics and deformation of the South American plate: insights from analog modeling. *Tectonics* 27, TC3011. <http://dx.doi.org/10.1029/2007TC002175>.
- Espurt, N., Baby, P., Brusset, S., Roddaz, M., Hermoza, W., Barbarand, J., 2010. The Nazca Ridge and uplift of the Fitzcarrald Arch: implications for regional geology in northern South America. In: Hoon, C., Wesselingh, F.P. (Eds.), *Amazonia, Landscape, and Species Evolution: A Look into the Past*. Wiley-Blackwell, Oxford, UK, pp. 89–100. <http://dx.doi.org/10.1002/9781444306408.ch6>.
- Eude, A., Roddaz, M., Brichau, S., Brusset, S., Calderon, Y., Baby, P., Soula, J.-C., 2015. Controls on timing of exhumation and deformation in the northern Peruvian eastern Andean wedge as inferred from low-temperature thermochronology and balanced cross section. *Tectonics* 34, 715–730. <http://dx.doi.org/10.1002/2014TC003641>.
- Forsyth, D.W., 1985. Subsurface loading and estimates of the flexural rigidity of continental lithosphere. *J. Geophys. Res. Solid Earth* 90, 12623–12632. <http://dx.doi.org/10.1029/JB090iB14p12623>.
- Gans, C.R., Beck, S.L., Zandt, G., Gilbert, H., Alvarado, P., Anderson, M., Linkimer, L., 2011. Continental and oceanic crustal structure of the Pampean flat slab region, western Argentina, using receiver function analysis: new high-resolution results. *Geophys. J. Int.* 186, 45–58. <http://dx.doi.org/10.1111/j.1365-246X.2011.05023.x>.
- Gautheron, C., Espurt, N., Barbarand, J., Roddaz, M., Baby, P., Brusset, S., Tassan-Got, L., Douville, E., 2013. Direct dating of thick- and thin-skin thrusts in the Peruvian Subandean zone through apatite (U–Th)/He and fission track thermochronometry. *Basin Res.* 25, 419–435. <http://dx.doi.org/10.1111/bre.12012>.
- Gutscher, M.A., Olivet, J.L., Aslanian, D., Eissen, J.P., Maury, R., 1999. The “lost Inca Plateau”: cause of flat subduction beneath Peru? *Earth Planet. Sci. Lett.* 171, 335–341. [http://dx.doi.org/10.1016/S0012-821X\(99\)00153-3](http://dx.doi.org/10.1016/S0012-821X(99)00153-3).
- Gutscher, M.A., Spakman, W., Bijwaard, H., Engdahl, E.R., 2000. Geodynamics of flat subduction: seismicity and tomographic constraints from the Andean margin. *Tectonics* 19 (5), 814–833. <http://dx.doi.org/10.1029/1999TC001152>.
- Hampel, A., 2002. The migration history of the Nazca Ridge along the Peruvian active margin: a re-evaluation. *Earth Planet. Sci. Lett.* 203, 665–679. [http://dx.doi.org/10.1016/S0012-821X\(02\)00859-2](http://dx.doi.org/10.1016/S0012-821X(02)00859-2).
- Hampel, A., Kukowski, N., Bialas, J., Huebscher, C., Heinbockel, R., 2004. Ridge subduction at an erosive margin: the collision zone of the Nazca Ridge in southern Peru. *J. Geophys. Res.* 109, B02101. <http://dx.doi.org/10.1029/2003JB002593>.
- Hasegawa, A., Nakajima, J., 2017. Seismic imaging of slab metamorphism and genesis of intermediate-depth intraslab earthquakes. *Prog. Earth Planet. Sci.* 4. <http://dx.doi.org/10.1186/s40645-017-0126-9>.
- Haxel, G.B., Jacobson, C.E., Wittke, J.H., 2015. Mantle peridotite in newly discovered far-land subduction complex, southwest Arizona: initial report. *Int. Geol. Rev.* 57 (5–8), 871–892. <http://dx.doi.org/10.1080/00206814.2014.928916>.
- Hermoza, W., Baby, P., Espurt, N., Martínez, E., Bolaños, R., 2006. The Ucayali Subandean basin: a complex fold and thrust belt and inverted system. In: *Bolivarian Symposium of Petroleum Exploration in the Subandean Basins*, 9th, Cartagena, Colombia.
- Hu, J., Liu, L., Hermosillo, A., Quan, Z., 2016. Simulation of late Cenozoic South American flat-slab subduction using geodynamic models with data assimilation. *Earth Planet. Sci. Lett.* 438, 1–13. <http://dx.doi.org/10.1016/j.epsl.2016.01.011>.
- Humphreys, E.D., Schmandt, B., Bezada, M.J., Perry-Houts, J., 2015. Recent craton growth by slab stacking beneath Wyoming. *Earth Planet. Sci. Lett.* 429, 170–180. <http://dx.doi.org/10.1016/j.epsl.2015.07.066>.
- International Seismological Centre, 2011. Online global earthquake bulletin database. <http://www.isc.ac.uk/iscbulletin/>, Accessed date: September 2016.
- Jacques, J.M., 2003. A tectonostratigraphic synthesis of the Sub-Andean basins: inferences on the position of South American intraplate accommodation zones and their control on South Atlantic opening. *J. Geol. Soc.* 160, 703–717. <http://dx.doi.org/10.1144/0016-764902-089>.
- James, D.E., Snoke, J.A., 1994. Structure and tectonics in the region of flat subduction beneath central Peru: crust and uppermost mantle. *J. Geophys. Res.* 99 (B4), 6899–6912. <http://dx.doi.org/10.1029/93JB03112>.
- Jamieson, R.A., Beaumont, C., 2013. On the origin of orogens. *Geol. Soc. Am. Bull.* 125 (11/12), 1671–1702. <http://dx.doi.org/10.1130/B30855.1>.
- Jordan, T.E., Allmendinger, R.W., 1986. The Sierras Pampeanas of Argentina: a modern analogue of Rocky Mountain foreland deformation. *Am. J. Sci.* 286, 737–764. <http://dx.doi.org/10.2475/ajs.286.10.737>.
- Kumar, A., Wagner, L.S., Beck, S.L., Long, M.D., Zandt, G., Young, B., Tavera, H., Minaya, E., 2016. Seismicity and state of stress in the central and southern Peruvian flat slab. *Earth Planet. Sci. Lett.* 441, 71–80. <http://dx.doi.org/10.1016/j.epsl.2016.02.023>.
- Liu, L., Gurnis, M., Seton, M., Saleeby, J., Müller, R.D., Jackson, J.M., 2010. The role of oceanic plateau subduction in the Laramide orogeny. *Nat. Geosci.* 3, 353–357. <http://dx.doi.org/10.1038/ngeo829>.
- Ma, Y., Clayton, R.W., 2015. Flat slab deformation caused by interplate suction force. *Geophys. Res. Lett.* 42, 7064–7072. <http://dx.doi.org/10.1002/2015GL065195>.
- Manea, V.C., Pérez-Gussinyé, M., Manea, M., 2012. Chilean flat slab subduction controlled by overriding plate thickness and trench rollback. *Geology* 40 (1), 35–38. <http://dx.doi.org/10.1130/G32543.1>.
- Margirier, A., Audin, L., Robert, X., Pêcher, A., Schwartz, S., 2017. Stress field evolution above the Peruvian flat-slab (Cordillera Blanca, northern Peru). *J. S. Am. Earth Sci.* 77, 58–69. <http://dx.doi.org/10.1016/j.jsames.2017.04.015>.
- Martinod, J., Husson, L., Roperch, P., Guillaume, B., Espurt, N., 2010. Horizontal subduction zones, convergence velocity and the building of the Andes. *Earth Planet. Sci. Lett.* 299, 299–309. <http://dx.doi.org/10.1016/j.epsl.2010.09.010>.
- McQuarrie, N., Barnes, J.B., Ehlers, T.A., 2008. Geometric, kinematic, and erosional history of the central Andean Plateau, Bolivia (15–17°S). *Tectonics* 27, TC3007. <http://dx.doi.org/10.1029/2006TC002054>.
- Molnar, P., England, P., 1990. Late Cenozoic uplift of mountain ranges and global climate change: chicken or egg? *Nature* 346 (6279), 29–34. <http://dx.doi.org/10.1038/346029a0>.
- Noury, M., Philippon, M., Bernet, M., Paquette, J.-L., Sempere, T., 2017. Geological record of flat slab-induced extension in the southern Peruvian forearc. *Geology* 45 (8), 723–726. <http://dx.doi.org/10.1130/G38990.1>.
- Picard, D., Sempere, T., Plantard, O., 2008. Direction and timing of uplift propagation in the Peruvian Andes deduced from molecular phylogenetics of highland biotaxa. *Earth Planet. Sci. Lett.* 271, 326–336. <http://dx.doi.org/10.1016/j.epsl.2008.04.024>.
- Porter, R., Gilbert, H., Zandt, G., Beck, S., Warren, L., Calkins, J., Alvarado, P., Anderson, M., 2012. Shear wave velocities in the Pampean flat-slab region from Rayleigh wave tomography: implications for slab and upper mantle hydration. *J. Geophys. Res.* 117, B11301. <http://dx.doi.org/10.1029/2012JB009350>.
- Portner, D.E., Beck, S., Zandt, G., Scire, A., 2017. The nature of slab slow velocity anomalies beneath South America. *Geophys. Res. Lett.* 44, 4747–4755. <http://dx.doi.org/10.1002/2017GL073106>.
- Pysklywec, R.N., Mitrovica, J.X., 2000. Mantle flow mechanisms of epeirogeny and their possible role in the evolution of the Western Canada Sedimentary Basin. *Can. J. Earth Sci.* 37, 1535–1548. <http://dx.doi.org/10.1139/e00-057>.
- Ramos, V.A., Folguera, A., 2009. Andean flat-slab subduction through time. In: Murphy, J.B. (Ed.), *Ancient Orogens and Modern Analogues*. Geological Society of London Special Publication, vol. 327. pp. 31–54. <http://dx.doi.org/10.1144/SP327.3>.
- Regard, V., Lagnous, R., Espurt, N., Darrozes, J., Baby, P., Roddaz, M., Calderon, Y., Hermoza, W., 2009. Geomorphic evidence for recent uplift of the Fitzcarrald Arch (Peru): a response to the Nazca Ridge subduction. *Geomorphology* 107, 107–117. <http://dx.doi.org/10.1016/j.geomorph.2008.12.003>.
- Rosenbaum, G., Giles, D., Saxon, M., Betts, P.G., Weinberg, R.F., Duboz, C., 2005. Subduction of the Nazca Ridge and the Inca Plateau: insights into the formation of ore deposits in Peru. *Earth Planet. Sci. Lett.* 239, 18–32. <http://dx.doi.org/10.1016/j.epsl.2005.08.003>.
- Ryan, W.B.F., Carbotte, S.M., Coplan, J.O., O'Hara, S., Melkonian, A., Arko, R., Weissel, R.A., Ferrini, V., Goodwillie, A., Nitsche, F., Bonczkowski, J., Zemsky, R., 2009. Global multi-resolution topography synthesis. *Geochem. Geophys. Geosyst.* 10 (3). <http://dx.doi.org/10.1029/2008GC002332>.
- Ryan, J., Beck, S., Zandt, G., Wagner, L., Minaya, E., Tavera, H., 2016. Central Andean crustal structure from receiver function analysis. *Tectonophysics* 682, 120–133. <http://dx.doi.org/10.1016/j.tecto.2016.04.048>.
- Sacke, V., Ussami, N., 2009. Reappraisal of the effective elastic thickness for the sub-Andes using 3-D finite element flexural modelling, gravity and geological constraints. *Geophys. J. Int.* 179, 778–786. <http://dx.doi.org/10.1111/j.1365-246X.2009.04334.x>.
- Schulze, D.J., Davis, D.W., Helmstaedt, H., Joy, B., 2015. Timing of the Cenozoic “Great Hydration” event beneath the Colorado Plateau: Th–Pb dating of monazite in Navajo volcanic field metamorphic eclogite xenoliths. *Geology* 43 (8), 727–730. <http://dx.doi.org/10.1130/G36932.1>.
- Scire, A., Zandt, G., Beck, S., Long, M., Wagner, L., Minaya, E., Tavera, H., 2016. Imaging the transition from flat to normal subduction: variations in the structure of the Nazca slab and upper mantle under southern Peru and northwestern Bolivia. *Geophys. J. Int.* 204, 457–479. <http://dx.doi.org/10.1093/gji/ggv452>.
- Scire, A., Zandt, G., Beck, S., Long, M., Wagner, L., 2017. The deforming Nazca slab in the mantle transition zone and lower mantle: constraints from teleseismic tomography on the deeply subducted slab between 6°S and 32°S. *Geosphere* 13 (3). <http://dx.doi.org/10.1130/G36932.1>.

- [org/10.1130/GES01436.1](http://dx.doi.org/10.1130/GES01436.1).
- Sébrier, M., Mercier, J.L., Macharé, J., Bonnot, D., Cabrera, J., Blanc, J.L., 1988. The state of stress in an overriding plate situated above a flat slab: the Andes of central Peru. *Tectonics* 7, 895–928. <http://dx.doi.org/10.1029/TC007i004p00895>.
- Somoza, R., Ghidella, M.E., 2012. Late Cretaceous to recent plate motions in western South America revisited. *Earth Planet. Sci. Lett.* 331–332, 152–163. <http://dx.doi.org/10.1016/j.epsl.2012.03.003>.
- Spikings, R., Simpson, G., 2014. Rock uplift and exhumation of continental margins by the collision, accretion, and subduction of buoyant and topographically prominent oceanic crust. *Tectonics* 33, 635–655. <http://dx.doi.org/10.1002/2013TC003425>.
- Stewart, J., Watts, A.B., 1997. Gravity anomalies and spatial variations of flexural rigidity at mountain ranges. *J. Geophys. Res. Solid Earth* 102, 5327–5352. <http://dx.doi.org/10.1029/96JB03664>.
- Tesauro, M., Audet, P., Kaban, M.K., Bürgmann, R., Cloetingh, S., 2012. The effective elastic thickness of the continental lithosphere: comparison between rheological and inverse approaches. *Geochem. Geophys. Geosyst.* 13 (9). <http://dx.doi.org/10.1029/2012GC004162>.
- Van Hunen, J., van den Berg, A.P., Vlaar, N.J., 2002. The impact of South-American plate motion and the Nazca Ridge subduction on the flat subduction below south Peru. *Geophys. Res. Lett.* 29, 35–1—35-4. <http://dx.doi.org/10.1029/2001GL014004>.
- Woods, M.T., Okal, E.A., 1994. The structure of the Nazca Ridge and Sala y Gomez seamount chain from the dispersion of Rayleigh waves. *Geophys. J. Int.* 117, 205–222. <http://dx.doi.org/10.1111/j.1365-246X.1994.tb03313.x>.
- Yonkee, W.A., Weil, A.B., 2015. Tectonic evolution of the Sevier and Laramide belts within the North American Cordillera orogenic system. *Earth Sci. Rev.* 150, 531–593. <http://dx.doi.org/10.1016/j.earscirev.2015.08.001>.